LUND UNIVERSITY
Faculty of Science

2*D* Neutron Imaging with ^{10}B -Based Multi-Blade Detector

Tõnu Ilves

Thesis submitted for the degree of Master of Science
Project duration: 4 months

Supervised by Kevin Fissum and Francesco Messi

Department of Physics
Division of Nuclear Physics
December, 2017

Abstract

In the field of thermal-neutron imaging, the Multi-Blade detector concept and design, being developed for the upcoming European Spallation Source in Lund, Sweden, is unique. The current report presents, for the first time, the neutron-imaging capabilities of a ^{10}B -based Multi-Blade thermal-neutron detector, measured at a reflectometry instrument at Rutherford Appleton Laboratory in Oxfordshire, England under high spallation neutron flux. This thesis is focused on producing two-dimensional neutron images from the measurements. A full overview of neutron-detection concepts and specifically, the Multi-Blade detector are given. The detector has excellent response to thermal neutrons. Detector short-comings are addressed and suggestions for a next wave of measurements and analysis are given.

Acknowledgements

The whole thesis project has been an unforgettable journey and an amazing privilege for me. For that, I would especially like to thank my colleagues in the Multi-Blade detector team that warmly took me on board: Francesco Messi (also my thesis supervisor), Francesco Piscitelli and Giacomo Mauri. Special gratitude to my supervisor Kevin Fissum for being the backbone of my work and an inspiration for my mind. My sincere appreciation to the whole Division of Nuclear Physics of Lund University for the warm welcome and assistance. I bow before my family and my close friends for an invaluable encouragement throughout my studies in Sweden. I dedicate this thesis to my biggest inspiration, motivation, support, and love - Juta.

Contents

List of Figures

List of Tables

List of Abbreviations

2D	2 Dimensional
BL	Beamline
COG	Center of Gravity
DAQ	Data Acquisition
DPP	Digital Pulse Process
ESS	European Spallation Source
HV	High Voltage
ILL	Institut Laue-Langevin
MB	Multi-Blade detector concept
MB-16	Specific Multi-Blade version
MWPC	Multi-Wire Proportional Chamber
QDC	Charge to Digital Converter
RAL	Rutherford Appleton Laboratory
S/N	Signal-to-Noise
STF	Source-Testing Facility
SWPC	Single-Wire Proportional Chamber
TOF	Time-of-Flight
TS	Time Stamp
UI	User Interface

Chapter 1

Introduction

1.1 The Neutron

1.1.1 Basics

Neutrons are electrically neutral subatomic particles that exist in a stable form when bound in the atomic nucleus together with protons [1]. Decades after the initial discovery of the neutron in the early 1930s [2], inner-structure studies have shown it to consist of one "up" and two "down" flavoured quarks. The intrinsic fractional electric charges[1] of the constituent quarks lead to charge neutrality. The resulting immunity to the Coulomb force makes neutrons excellent probes for matter. Nuclear reactions and scattering are the main channels for interaction.

Neutrons that are not confined inside a nucleus are referred to as being "free". Free neutrons are unstable and decay. A free neutron mean lifetime is about 15 minutes, which is a significant amount of time to interact with matter. The characteristics of the neutron interaction are strongly energy E_n dependent, and arise from its wave-like properties. At room temperature[2] $E_n = 20$ meV, the neutron wavelength[3] is 1 Å and the mean velocity is 2.2 km/s.

The size of the atomic nucleus is on the order of 10^{-15} m, which on terms of the size of an atom is small. This suggests a relatively low probability for free neutrons to undergo a scattering reaction in the matter. The general transparency of even dense matter to neutrons makes them excellent probes but also biologically hazardous [4]. Further, it is difficult to detect them.

1.1.2 Energy

In an atomic nucleus, neutrons are bound. This gives rise to a threshold energy value $E_{b,n}$ which needs to be externally provided in order to free them. This can be achieved by

[1] up: $+\frac{2}{3}e$, down: $-\frac{1}{3}e$, e stands for elementary electric charge unit [3].
[2] Room temperature is considered to be at around 290 K.
[3] the size of an atom 10^{-10} m.

bombarding low $E_{b,n}$ elements with γ-rays, electrons, other nucleons or even nuclei [1, 5]. Nuclear reactors and spallation sources produce free neutrons with wide energy spectrum E_n.

E_n defines the wavelength of the neutron. By expressing $E_n = \frac{p_n^2}{2m_n}$ and combining it with de Broglie formula $p_n = \frac{h}{\lambda_n}$, the equivalence can be seen

$$E_n = \frac{p_n^2}{2m_n} = \frac{h^2}{2m_n\lambda_n^2} \propto \lambda_n^{-2}, \tag{1.1.1}$$

where p_n is the neutron momentum and h is Planck's constant. Neutrons at room temperature, also referred to as thermal neutrons, have a wavelength λ_n which is comparable to the size of an atom. By fixing E_n and directing neutrons onto a material, the properties of the material on the length scale of λ_n may be studied. In Table 1.1.1, a rough classification of neutron energies and corresponding length scales is given[4].

Type	E_n	λ_n	
Cold neutrons	$\simeq 2.2$ meV	6.1 Å	$> 10^{-10}$ m
Thermal neutrons	$\simeq 20$ meV	1 Å	$\sim 10^{-10}$ m
Epithermal neutrons	$\simeq 1$ eV	0.3 Å	$\sim 10^{-11}$ m
Fast neutrons	> 0.1 MeV	10^{-6}Å	$\sim 10^{-16}$ m

Table 1.1.1. Neutron energies and corresponding wavelengths. Thermal neutrons are in thermal equilibrium with their surroundings at room temperature.

Neutrons can interact with a target nucleus through elastic or inelastic scattering or via nuclear reactions. The probability for and type of neutron interaction is strongly dependent on E_n. In general, the longer the neutron spends near the target nucleus, the higher the probability to undergo a nuclear reaction [1]. The absorption cross section has an inverse dependence on velocity and thus absorption becomes more probable for lower velocities. Slowing neutrons down is accomplished via a process called "moderation". Detecting nuclear-reaction fragments from neutron-induced interactions is the main neutron-detection concept presented in this thesis.

At thermal energies, neutron absorption dominates over scattering. There are some isotopes that exhibit remarkably large absorption cross sections at thermal energies. These are ^{3}He, ^{10}B, and ^{6}Li. Their respective neutron-interaction probabilities or "cross sections" are plotted in Fig. 1.1.1 as a function of energy. It can be seen that thermal-neutron absorption for these elements exceeds fast-neutron absorption by four orders of magnitude. The cross section profiles are smooth and have no resonances in the thermal-energy range. This makes these elements desirable as detector media. In terms of the absorption cross section, ^{3}He is superior and has thus been the traditional choice for neutron detectors for decades. The recent shortage of this element has forced the scientific community to look for alternatives [6].

[4]In this thesis, thermal neutrons are of most interest. Thus, if not specified otherwise, "neutron" always refers to a thermal neutron.

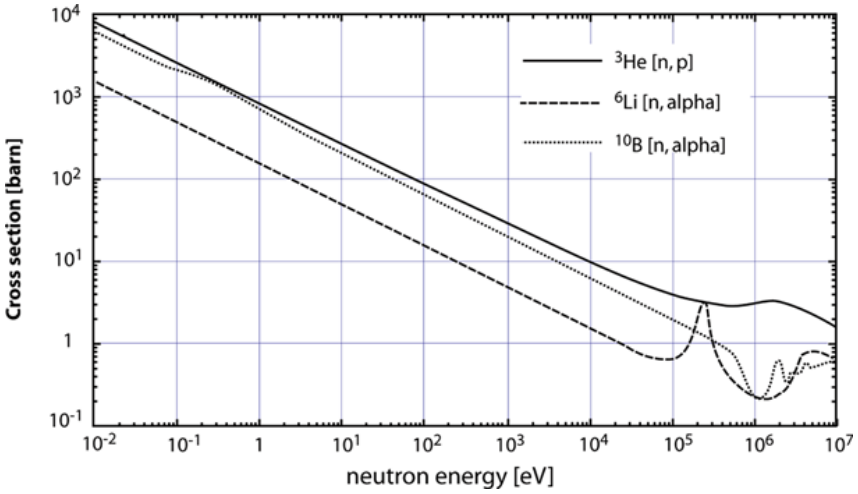

Figure 1.1.1. Neutron capture cross sections. For ^{3}He, ^{6}Li, and ^{10}B. The square brackets next to the isotopes in the legend denote the probe (first element) and detected product (second element) for the nuclear reaction in question. The cross section is given in barns (1 b = 10^{-28} m^2). Image taken from Ref. [5].

The neutron absorption cross section for a nuclear reaction also depends on the density of the target material. Thus, both the element and the density of the element are important for capturing neutrons.

1.1.3 Detection

The charge neutrality of neutrons makes their detection difficult. All modern particle monitoring systems deal with electrical signals. The presence of neutrons may be detected indirectly by measuring the charged nuclear-reaction fragments that are released after the material absorbs the neutron. These neutron-absorbing materials are referred to as "converters". The charged reaction products that converters produce initiate the electrical-signal formation, generally in an electric field. Devices based upon such techniques are called "ionization" detectors.

Multi-Wire Proportional Chamber

This thesis reports on an ionization chamber that uses a gas as the ionization medium for the nuclear-reaction fragments. The simplest of such detectors is a cylindrical chamber with a conductive central wire and conductive walls, see Fig. 1.1.2. A positive electric potential $+V_0$ relative to the walls is applied to the wire, making the wire an anode and the walls cathodes [7]. With such a configuration, a radial electric field in the cylinder is established

$$E = \frac{1}{r} \frac{V_0}{\ln(b/a)}, \tag{1.1.2}$$

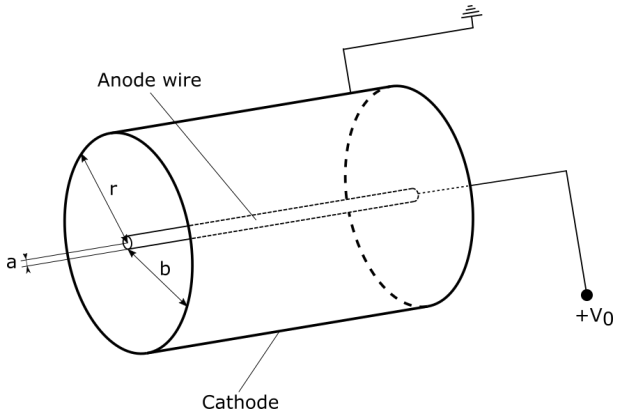

Figure 1.1.2. Single-wire proportional chamber. A cylindrical ionization chamber for detecting charged particles through gas ionization is shown. The grounded walls of the detector have a negative potential relative to the central anode wire.

where r is the radial distance from the wire and b, a are the cylinder and wire radii respectively. The charged reaction products traverse the gas volume and start colliding with the gas molecules in an applied electric field. The reaction fragments free electrons from gas molecules via collisions in the process called ionization. The first electrons that are created in the ionization process are referred to as "primary" electrons, and these can themselves produce further ionization referred to as "secondary" electrons. This leads to an electron "avalanche" near the anode and results in signal formation on the wire. The signal generated on the electrodes is formed as a result of the movement of the charges rather than by physical collection of the charges themselves [7]. Electrons are lighter than ions and therefore arrive at the anode earlier than the ions arrive at the cathode. This ion-cathode time interval from a single neutron event is important for event reconstruction, see Sect. 3.4.2.

The charge-collection dependency on applied voltage V_0 is shown in Fig. 1.1.3. When V_0 is too low, no charge collection takes place because electron-ion pairs recombine under their own attractive electrical field. Sufficiently high V_0 is therefore needed, not only to overcome recombination forces, but also to amplify the relatively weak signal. This is achieved in the "proportional counter" regime, where the voltage V_0 applied to the anode can be somewhere between 0.7 – 2.4 kV. The amplification or gain for each individual electron or ion in the gas is constant throughout the proportional regime, because of the almost linear correlation between the number of ions collected and V_0. The amplitude of the output signal is proportional to the liberated primary ionization in the gas and thus to the fragment energy [5]. If the applied voltage in the chamber is correctly adjusted, the average charge collected by the detector in the ionization process is proportional to the reaction-fragment energy. These detectors are called proportional counters, making the detector in Fig. 1.1.2 a single-wire proportional chamber (SWPC).

The gas medium for proportional counters is usually a mixture of a noble gas and a polyatomic gas. Noble gases such as Ar produce electron cascades with the lowest electric-

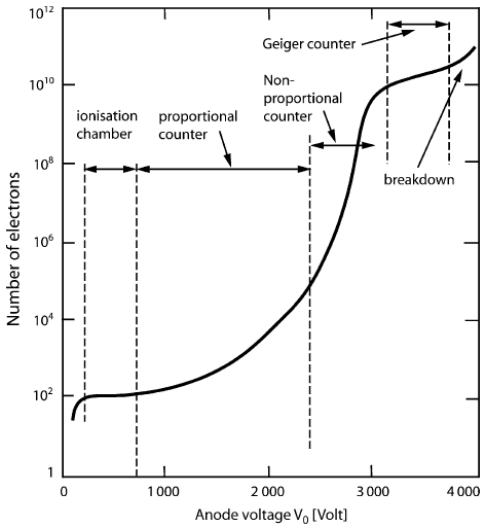

Figure 1.1.3. Charge-collection dependency on V_0. Sections in between dashed lines represent different working regimes. The proportional regime spans from 700 V to post 2.4 V. Image from [5].

field intensities and offer good proportionality at high rate. However, pure Ar gas can produce discharge between the electrodes due to further electron avalanches caused by the energetic γ-rays that Ar atoms emit when they de-excite. Thus, a "quencher" gas is needed to prevent the discharge by absorbing these emitted γ-rays. Polyatomic gases such as CO_2 have many degrees-of-freedom and are excellent quenchers, providing a wide range of energy levels for the γ-rays to be absorbed [7]. The choice of the gas-mixture ratio is correlated to the applied voltage V_0. A higher quenching gas concentration generally has to be balanced with higher V_0 if the same gain is desired.

An extension to the SWPC is the multi-wire proportional chamber (MWPC), invented by Charpak in 1968 [8]. The MWPC is in principle a series of SWPCs, but exhibits a different electric-field geometry having a series of parallel wires in a single gas volume, see Fig. 1.1.4. The cathode planes are often segmented into thin strips that are orthogonal to the anodes. In this way, it is possible to determine spatial coordinates of signals in two dimensions. Apart from V_0, the gain of the signal in a MWPC also depends on the gas

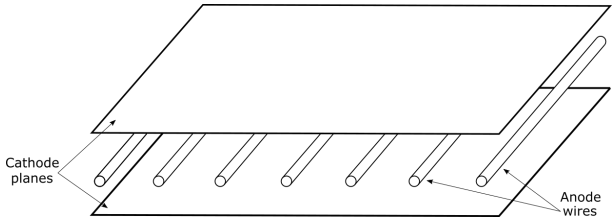

Figure 1.1.4. Multi-wire proportional chamber. Series of wires reside between two cathode planes. The cathode planes can be segmented into strips.

mixture in the chamber, the gas-mixture ratio, the pressure of the gas, the electric-field geometry, and the charge of the liberated ions. Such variables are detector specific and discussed in detail in Sect. 2, where neutron-detection features, exemplified by ^{3}He and ^{10}B converters, are presented.

^{3}He-Based Neutron Detection

^{3}He-based neutron detectors can be proportional tubes, see Fig. 1.1.2. The tube is filled mostly with ^{3}He and ∼5% quenching gas [5]. An incoming neutron penetrates the tube wall and undergoes a nuclear reaction with the ^{3}He gas accordingly to

$$^3\mathrm{He} + n \rightarrow {}^3\mathrm{H} + p \quad ; \quad Q = 0.764\,\mathrm{MeV}, \tag{1.1.3}$$

where ^{3}H is tritium, p is a proton and Q is the energy[5] released in the process. The reaction products ionize the ^{3}He gas and the liberated primary and secondary electrons collectively move towards the anode wire and induce a signal on the wire. Here, ^{3}He acts simultaneously as a neutron converter and a medium for liberated electron-ion pairs. The natural abundance of ^{3}He among all the helium isotopes is 137 ppm[6]. This is extremely low, forcing commercial production of the element. ^{3}He was a by-product of the nuclear-weapon industry during the Cold War era [6]. As nuclear-weapon production is not taking place on the Cold War scale any longer, the scarcity of the substance has drastically inflated the cost. Thus, alternative elements are being investigated for replacing ^{3}He.

^{10}B Based Neutron Detection

In the thermal-energy range, ^{10}B is one of the best alternatives to ^{3}He. Even though its absorption cross section is 28% smaller than ^{3}He, it is still significant at 3840 b [5]. The natural abundance of ^{10}B is 19.9%, which makes it economically affordable. The two main ^{10}B neutron-absorption nuclear reactions are:

$$\begin{aligned} {}^{10}\mathrm{B} + n &\xrightarrow{94\%} {}^7\mathrm{Li}^* + \alpha = {}^7\mathrm{Li} + \alpha + \gamma(0.48\,\mathrm{MeV}) \quad ; \quad Q = 2.792\,\mathrm{MeV} \\ {}^{10}\mathrm{B} + n &\xrightarrow{6\%} {}^7\mathrm{Li} + \alpha \quad ; \quad Q = 2.312\,\mathrm{MeV}\,, \end{aligned} \tag{1.1.4}$$

where α is a ^{4}He nucleus [1, 9]. The asterisk in ^{7}Li* denotes the first excited state, which decays with a lifetime of $\sim 10^{-3}$ s to its ground state by emitting a 0.48 MeV γ-ray. The fragments ^{7}Li and α are ejected almost exactly back-to-back in the center-of-momentum frame [5]. ^{10}B as a converter can be either a gas or a solid[7]. If solid, only a very thin layer can successfully be used, or else the reaction products will not escape the layer. The higher Q-value for ^{10}B is advantageous when using solid ^{10}B. Due to the random direction of ejected fragments and energy loss and escape mechanism in the ^{10}B, the deposited-energy profile in the gas is continuous and ranges from zero to the maximum energy carried by the fragment [10]. Note also that events that deposited energy that might have come also from a γ-ray must be rejected [9].

[5] The reaction Q-value manifests itself as the kinetic energy of the reaction products [9].

[6] ppm - parts per million.

[7] At room temperature, ^{10}B is in the solid state.

Chapter 2

Multi-Blade ^{10}B-Based Detector

2.1 Multi-Blade Detector Concept

The Multi-Blade (MB) neutron detector has been designed and built for the European Spallation Source (ESS) which is currently under construction in Lund, Sweden. ESS is going to be a world-leading pulsed-neutron spallation source with unparalleled power [11]. this will set stringent requirements for the detectors. MB is designed for neutron reflectometry[8] instruments [13], which demand high spatial resolution and high count-rate tolerance in their detectors. The first MB concept was proposed at the Institut Laue-Langevin (ILL) in 2005 [14], utilizing MWPC detection principles and solid ^{10}-based neutron interactions. Since 2012, four separate detector prototypes have been built and tested [10]. Within 5 years, the MB project has gone through several upgrades. Here, the latest version prototype referred to as MB-16, is introduced.

All current MB detector versions are gas-filled ionization chambers that employ an array of identical "blades". As illustrated in Fig. 2.1.1, each blade has a "strip" plane underneath and $^{10}B_4C$-coated solid layer on top. The thin ^{10}B component of the $^{10}B_4C$ coating is the neutron converter. The strips are a grid of 32 parallel conductive straps. The blades are grounded, and thus the strips and the converter act as cathodes. Between the blades resides an orthogonal grid of 32 anode wires. The B_4C coating of a blade, together with the nearby wire and the corresponding strip plane function as a MWPC and act as a unit known as a "cassette"[9].

The incoming neutrons undergo a nuclear reaction inside the flat solid ^{10}B layer and at most one reaction fragment escapes into the gas medium. Upon escape, the fragment starts to ionize the gas and the first primary electrons are accelerated toward the closest anode. Each cassette is read-out independently and the corresponding blade acts as an active area, where mutually orthogonal wires and strips determine the x-and y-planar coordinates of the neutron reaction. MB-16 has 9 cassettes, each consisting of 32 equally

[8] Reflectometry is a technique for investigating material surfaces and interfaces through wave reflection [12].

[9] Note that this definition for a cassette is only used in the present thesis and due to changes in detector design it may differ from the definitions given in previous and forthcoming publications.

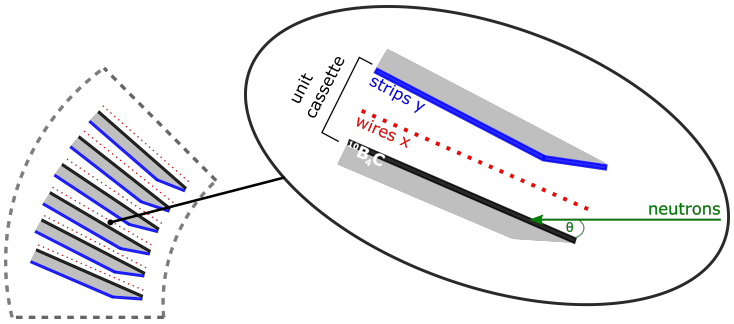

Figure 2.1.1. Top view of the MB detector with a zoom-in into one of the identical constituent units - a cassette. There are several cassettes in an array, which are forming an angle θ relative to the incident n-beam. The angle θ is unique for each blade while the blades themselves are not exactly parallel to each other.

spaced wires and strips. This 4 mm mutual spacing of the wires and the strips gives the first-order spatial resolution in the x and y directions. Due simply to the higher pitch, the smaller the wire or strip spacing, the better the spatial resolution. However, the wires cannot be placed infinitely close to one another, as this would result in distortions and mechanical problems. The spatial resolution for the wires is instead increased geometrically by the 5° inclination of the blades relative to the incoming neutrons, see Fig. 2.1.2.

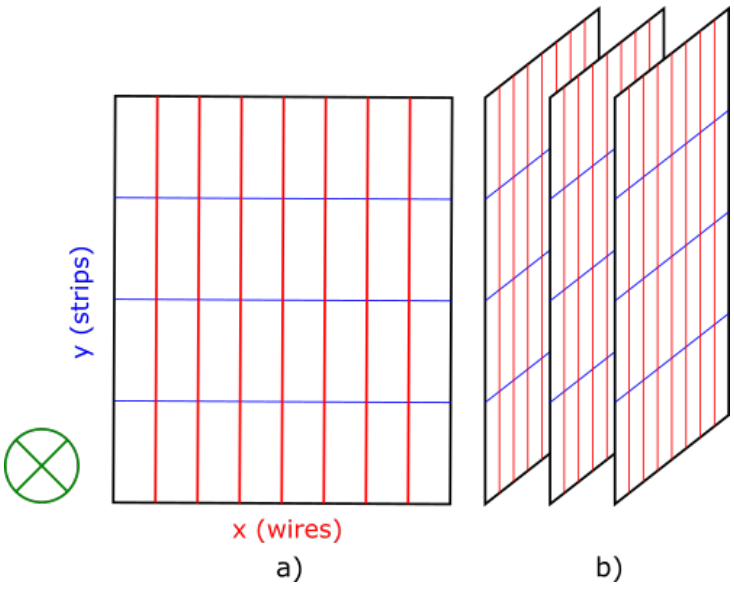

Figure 2.1.2. Projection of the wire pitch. Two different cassette alignment cases relative to the incoming neutron beam (indicated by the green symbol). Red lines are the wires and blue lines are the strips. Notice the higher density in the wire spacing if its projection in x axis is used. Also note how strip projection in the y axis will be unaffected.

This way, the wire pitch from the neutron frame-of-reference is the projection of the actual physical wire pitch. At $\theta = 5°$, the packing density of the wires is thus improved by a factor of $\sim$11. It has been shown that $\theta = 5°$ is the optimal angle. Below 5°, the converter efficiency starts to decrease due to increasing neutron reflection from the ^{10}B coating. The angle θ also improves the detector count-rate performance because the incident neutron flux is shared between more wires [10, 13, 15].

The blades are designed to physically overlap one another when at a 5° angle. This means that the downstream part of the ^{10}B coating of a blade is "shadowed" by an upstream blade. This is done to avoid "dead zones" where neutrons can otherwise pass through and escape [13]. Knowledge of the number of wires being shadowed allows for fine tuning the MB detector alignment with respect to the incoming neutron beam. To keep the optimal 5° alignment angle, the blades are positioned in an arc formation to form an offset angle relative to each other, see Fig. 2.1.3. The detector has been engineered for a position 4 m away from the sample, resulting in a 0.19° compensation angle between the blades. In this way, the shadow areas for the blades are equal. If the MB is properly aligned, 4 wires are shadowed by each blade. If the detector is closer or further away from

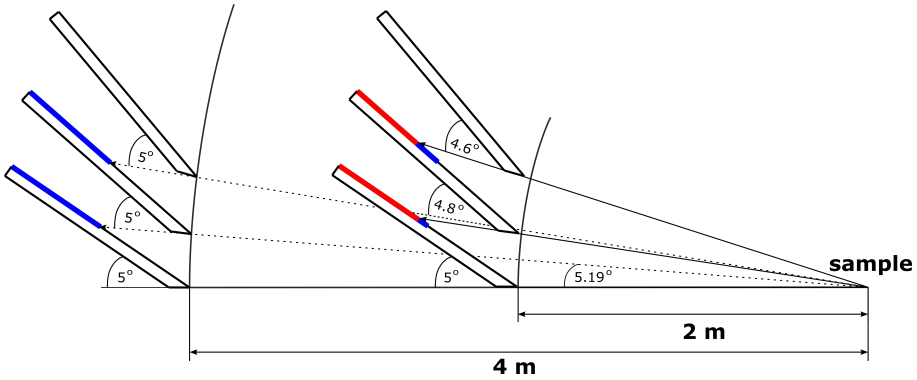

Figure 2.1.3. Alignment of the blades. At 4 m from the sample, the detector blades are aligned in an arc formation with a mutual 0.19° offset angle. The blue area indicates the shadow if the blades are at an optimal distance, whereas the red is the shadow area if the detector is closer to the sample.

the optimized detector-to-sample distance, only one blade can be aligned to the design specification of 5°, resulting in an increasing misalignment for subsequent blades. This is depicted in Fig. 2.1.3. In such a way, the shadow area also varies as function of blade.

As an ionization medium, MB-16 uses an $ArCO_2$ gas mixture which is held slightly above 1 atm. The MB-16 is flexible to the inert-to-quenching gas ratio, and the response of each electrode can be uniquely assigned. In this work, $ArCO_2$ blends with ratios of 80/20 and 70/30 were used.

2.1.1 Electronics

An illustration of the electronics readout sequence is given in Fig. 2.1.4. Each channel of the MB-16 has its own individual signal amplification on two pre-amplifier boards per cassette. The charge-sensitive pre-amplifier shapes and integrates the differential current

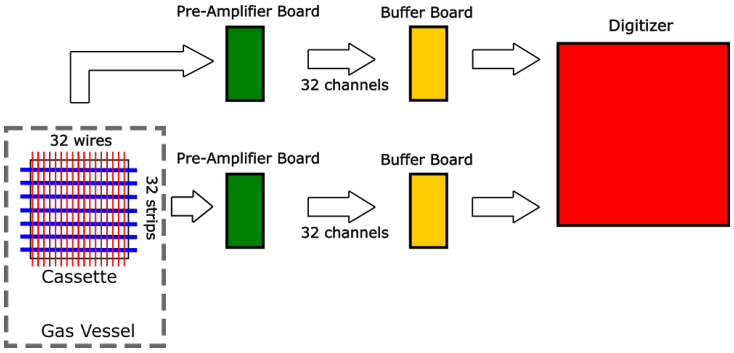

Figure 2.1.4. An MB-16 electronics for one cassette. The red lines are the wires and blue lines the strips in the gas vessel. Each board hosts 32 channels.

pulse $i = dq/dt$ resulting in the total charge Q of the pulse[10]. The output is an amplified analogue voltage signal V_{out} that is proportional to Q. The pre-amplifier thus acts as a charge-to-voltage converter. Two "buffer" boards per cassette are connected to the pre-amplifiers. A buffer is used to match the 50 Ω output signal impedance to the commercial digitizer impedance. After the buffer, the amplified analogue voltage signal is fed into a digitizer, where the charge-to-digital conversion (QDC) takes place.

2.1.2 Signal Acquisition

The 64 channel QDC for a single cassette is performed with a module called a "waveform digitizer" [16]. It is a device similar in principle to a digital oscilloscope: an electrical analogue signal is sampled with a high rate. The output, a stream of digital values, is sequentially stored into a circular "memory buffer"[11]. The working cycle of the digitizer is depicted in Fig. 2.1.5. A CAEN Model V1740D was used. The analog signal sampling rate is 62.5 MHz, which gives $1/62.5 \times 10^6 = 16$ ns steps between each sample point. Each sample point has a digital value equivalent to the voltage as well as a cumulative Time Stamp (TS) that addresses the sample point. The time-tagged digital-sample values are temporarily stored in a memory buffer of selectable length. If one of the samples stored in the buffer exceeds a selected threshold value, a "trigger"[12] event is executed and the memory buffer will freeze, allowing for user-defined number of previous sample instances

[10] The integration is performed over the time duration of the signal $V_{\text{out}} \propto Q = \int_0^t i dt$.

[11] A piece of electronics where the data is temporarily stored.

[12] The point in time at which a repeating signal acquisition window of waveform information is stabilized for viewing [17].

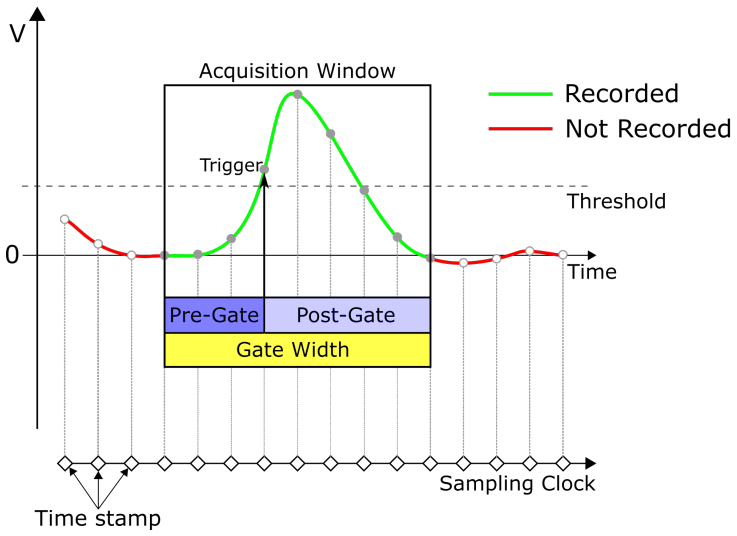

Figure 2.1.5. Digitizer signal acquisition. The vertical axis is the voltage, which has a threshold value to initialize the trigger. The upper horizontal axis represents time while the lower horizontal axis represents the sampling clock, which addresses each sample with a time stamp. The spacing between the samples is 16 ns. The green waveform represents the pulse that is eventually integrated. The samples in red are ultimately overwritten.

to be captured. If no trigger occurs, the memory of the buffer is simply overwritten with new sample values.

A digital-pulse process (DPP) is initiated after a trigger occurs. A predefined time delay or "pre-trigger" determines the time interval also known as a "pre-gate" in which the measured samples are associated with the triggered event. Similarly, a predefined time interval after the trigger known as a "post-gate" associates subsequent sample values with the trigger event. These time intervals together form an "acquisition window" whose length is called the "gate", see Fig. 2.1.5. All the sample values within an acquisition window form a pulse with a pre-trigger time stamp. The length of the pulse is a variable under different conditions. The width of the pulse is determined during detector calibration. The pulse is then passed to the charge-to-digital conversion (QDC) process where the sample values are integrated, resulting in a voltage value that is proportional to the accumulated charge of the signal.

CAEN digitizer modules are designed to be synchronized to each other [18]. They can be cascaded by distributing a common clock reference to all of the QDC sampling clocks. This allows coherent data acquisition (DAQ) between all of the individual channels. By employing programmable trigger logic and correlated time stamps, neutron-signal coincidences between nearby channels can be implemented. This is the main principle upon which MB neutron imaging is based.

Chapter 3

Measurements at the Rutherford Appleton Laboratory

3.1 Preliminary Preparation

During the first week of October 2017, a series of measurements with MB-16 were carried out at the pulsed-neutron facility called ISIS at Rutherford Appleton Laboratory (RAL) in Oxfordshire, England. The aim of the measurements was to test for the first time the MB-16 detector performance using an actual instrument. ISIS is an accelerator-based spallation-neutron source, where neutrons are generated by bombarding a tungsten target with high-energy protons. The protons are initially accelerated to 800 MeV energy in a synchrotron, which is a circular-shaped particle accelerator [19]. These protons are then directed onto a neutron-rich W target, resulting in an isotropic neutron[13] field. The target is surrounded by a moderator where the spallation-neutron energy, through inelastic scattering, is dramatically reduced. Neutrons leaving the moderator are guided to beamlines (BL). One of these BLs was CRISP where MB-16 was tested.

One month prior arriving at RAL, all the relevant parts of the MB-16 detector were tested at the Source-Testing Facility at Lund University [20]. The responses of all the channels of the blades were tested relative to background and to actinide-Be neutron source. During the tests, the detector gas was $ArCO_2$ 80/20, which required sub-kV HV for a reasonable signal-to-noise (S/N) ratio. In order to facilitate the tests, a UI was written. The UI allowed faster precision parameter modification in the configuration file. The UI was extensively used in all of the measurements at ISIS. The UI is described in detail in Appendix C.

3.2 Experimental Setup

At ISIS, the experiments were carried out on the neutron-reflectometry BL CRISP. BL schematics are shown in Fig. 3.2.1. At CRISP, moderated neutrons ($\geqslant 0.5$ Å) were directed

[13] Amongst other radiations, in particular large numbers of γ-rays are emitted.

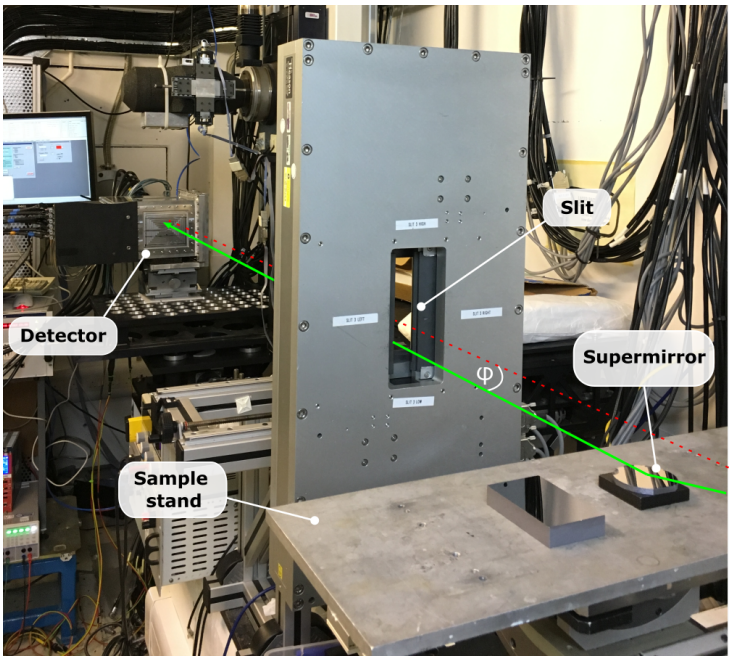

Figure 3.2.1. CRISP BL schematics. The neutron beam is depicted with the green arrow. The reflection is done at a grazing angle ϕ, highlighted by the red dashed line that is parallel to the floor.

onto a supermirror[14] located on a sample stand. The moderator-to-detector distance was 12 m and the detector-to-sample distance was ∼2 m. The incoming neutrons were pre-collimated with maximum beam dimensions of 40 × 10 mm^2, for width and height respectively. The user-accessible BL room was equipped with 3 electrically adjustable slits for further collimation, see Fig. 3.2.1 [22].

3.2.1 Detector Assembly

The MB is designed for neutron reflectometry where high resolution is demanded only in one dimension. As described in previous section, CRISP is a reflectometer[15], where the sample geometry is horizontal. However, MB-16 is designed for vertical reflectometry instruments. As a result, the detector had to be rotated 90° relative to its normal design configuration. The wires were thus orthogonal to the incoming neutron beam so that the wire pitch projection principle could be used, recall Fig. 2.1.2.

MB-16 was mounted onto a movable metal platform, see Fig. 3.2.2. The detector apparatus was fixed with plastic plates on either side of the platform to isolate the MB-16 metal chassis from the CRISP BL aparatus. To obtain the desired 5° blade alignment with respect to the reflected beam, a wedge was inserted underneath the detector. A goniometer was installed on top of the wedge for fine-tuning. The detector was mounted onto the

[14]Supermirrors are multilayered surfaces of two materials that facilitate neutron reflection at small grazing angles [21].

[15]Reflectometer and reflectometry BL phrases can be used interchangeably.

goniometer in the sideways position. In such a way, the strips lie parallel and the wires

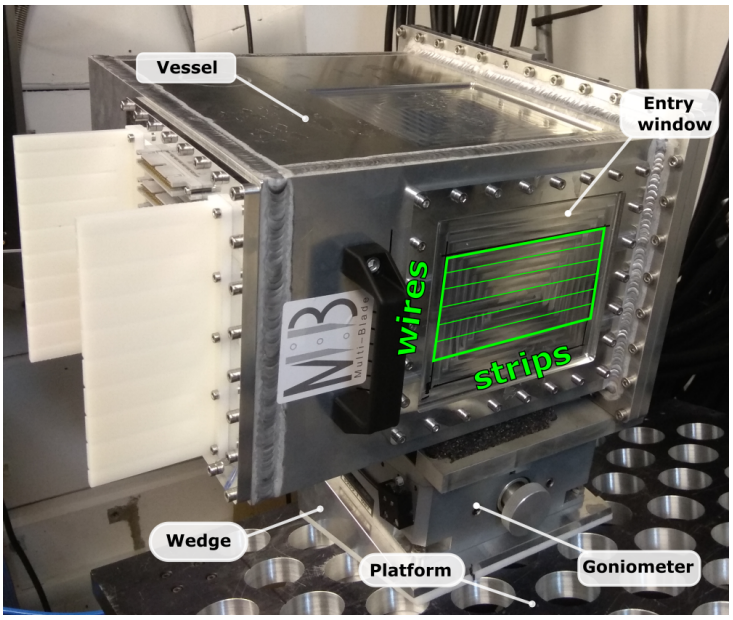

Figure 3.2.2. Detector assembly. The region in green represents detector active area, where the cassette placement is highlighted.

lie horizontal with respect to the lab floor, see Fig. 3.2.2. The detector was continuously flushed with $ArCO_2$ 70/30 gas at a pressure slightly above 1 atm. Of the 9 cassettes, the top 6 were connected to digitizers, while the bottom 3 were not. The digitizer clocks were mutually synchronized as well as synchronized to the facility neutron-pulse reference to reset the time stamp after each beam pulse.

3.2.2 Calibration

With a total of $6 \times 64 = 384$ channels, the neutron-sensitive area of the MB was 61 mm in the wire direction and 124 mm in the strip direction, see Fig. 3.2.2. Hardware thresholds just above the level of electric noise were set with no beam. The MB alignment was calibrated with a 40×1 mm^2 collimated neutron beam. The beam was directed onto the transition area between two bottom blades and adjusted until a four-wire shadow area was achieved. This corresponded to the 5° angle with respect to the neutron beam. At CRISP, the detector-to-sample distance was 2.33 m. Thus, only one blade could be aligned to the 5° angle while the other blades were decreasingly offset at smaller and smaller angles, recall the Fig. 2.1.3. The applied voltage was 1.3 kV.

3.3 Selected Measurements

This thesis presents the 2D imaging reconstructions from two of the neutron-absorbing boron carbide (B_4C) mask measurements performed during the one-week test at RAL.

The goal was to reproduce the image of the engravings with the detector. In these measurements, the active detector area was covered with neutron-absorbing masks. As previously mentioned, the masks were illuminated with the neutron beam which was reflected from a neutron supermirror located 2.33 m upstream. The masks were assumed to absorb 100% of incident neutrons. To fully irradiate the mask with the neutrons, a beam scan was necessary. The angle of the supermirror was varied using a programmable motorized sample stand.

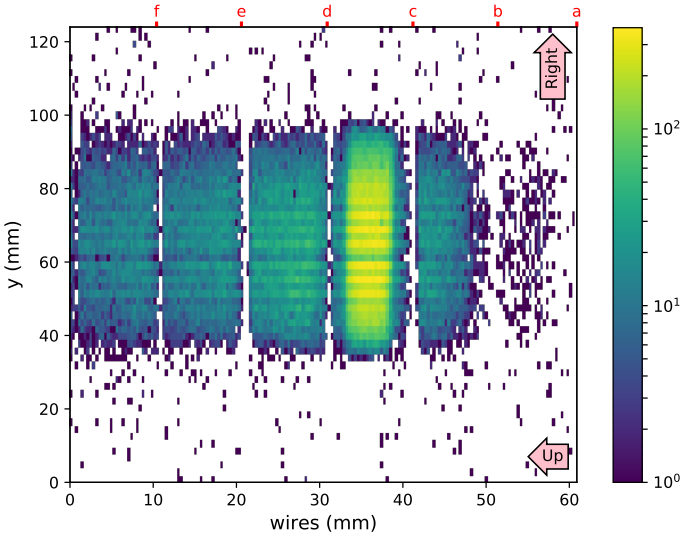

Figure 3.3.1. Divergent neutron-beam profile. The beam profile is given in logarithmic scale. The beam is obtained through reflection from a supermirror. The pink arrows represent the laboratory coordinates of the MB-16.

To maximize the area irradiated by the neutrons, a divergent 40×10 mm^2 beam was used. The reflected neutron beam profile rotated by 90° is shown in Fig. 3.3.1. The beam spread in the x-direction is a characteristic of the reflection as the reflected neutron angle is a function of λ_n. A complete discussion of the features seen in the Fig. 3.3.1 are discussed in Sect. 4.

As previously mentioned, two masks were chosen for this thesis. They are shown in Fig. 3.3.2. CAD drawings of the masks are presented in Appendix B. The widths of the etchings in the masks were not equal, and thus the finer detailed engravings were aligned with the wires. In a single measurement, the reflected neutron beam was scanned across the engravings twice by using a down/up movement. The initial and final position of the scan was at cassette "f" seen in Fig. 3.3.1. Since the DAQ and the motorized sample stand were independent systems, the start and stop of both the scan and DAQ were done manually.

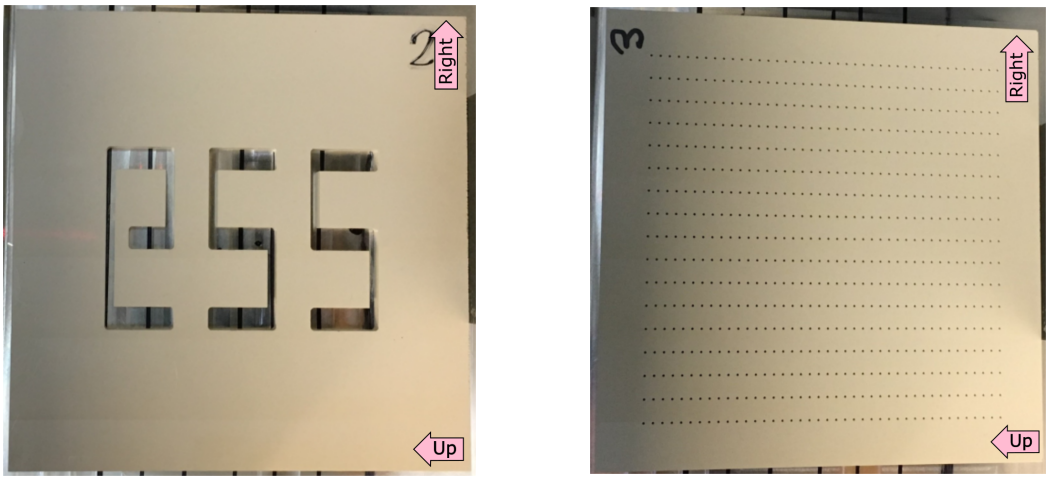

(a) ESS mask close-up. **(b)** Dotted mask close-up.

Figure 3.3.2. The B_4C masks. Both images are rotated by 90° relative to the measurement setting, indicated by the pink arrows.

3.4 2D Imaging Technique

3.4.1 Filtering Data

Digitizers provided the time stamp, the channel number and the charge of the signal if it exceeded the channel-specific threshold value, recall Sect. 2.1.2. A time stamp was assigned to each signal with reference to the 50 Hz proton beam. The digitizer time stamp counter reset every time a proton pulse hit the target, with the clock reference provided by the ISlS facility. Thus, within $1/50 = 20$ ms, a signal received a uniquely addressed time-of-flight (TOF) value. The TOF defined the kinetic energy of the incoming neutron because the distance from the spallation target to the detector was known

$$E_{k,n} = \frac{m_n v_n^2}{2} = \frac{m_n}{2} \cdot \left(\frac{d}{t_{\mathrm{TOF}}}\right)^2 \quad \Rightarrow \quad t_{\mathrm{TOF}} = d\sqrt{\frac{m_n}{2E_{k,n}}}, \tag{3.4.1}$$

where v_n is the neutron velocity, m_n is neutron rest mass and d is the distance the neutron travels from the target to the detector.

The MB-16 detector was optimized for detecting thermal neutrons, but it can in principle detect neutrons of all energies as well as γ-rays. At the instant of the interaction between the proton beam pulse and the W spallation target, γ-rays are promptly emitted. By blanking the first few milliseconds from each neutron pulse, this prompt γ-ray background was dramatically reduced, allowing the exact specification of the incident E_n range. The thermal-neutron energy is in the range of $E_n \leqslant 20$ meV, recall Table 1.1.1. Using the $E_n = 20$ meV upper limit value and $d = 14.33$ m in Eq. (3.4.1) results in the highest energy thermal neutrons arriving at $t_{\mathrm{TOF}} \simeq 6$ ms after the pulse-target impact. This 6 ms lower time threshold value was applied to all of the data sets in the present

thesis. Signals with recorded charge lower than 3500 ADCch[16] were also filtered from the data. Note that this value is actually lower for the first wires of each cassette, discussed in Sect. 4.1.3. The limit is applied to reduce the probability of detecting a signal from a γ-ray.

3.4.2 Clustering

The digitizers recorded signals for every channel. However, as was shown in [10], having a single hit in a wire and a single hit in a nearby strip from a single neutron is a very special case. More generally, within certain time Δt, many wires and strips together can produce a series of signals. Recombining the hits that came from a single neutron is called "clustering". This is the basis of the image reconstruction. To first order, signal clusters have to be defined by time. The drift time of the positive ions from the ^{10}B layer to the cathodes defines the time interval Δt of the cluster. Every hit within Δt corresponds to the same time cluster. In the present work, the time clusters were defined with $\Delta t = 3$ μs [23].

Within time cluster, channels hit consecutively form a wire or a strip sub-cluster. For a 1.47 MeV α particle, the maximum range in 1 atm $ArCO_2$ gas is around 8 mm. This is two channel-spacing units. As a result of the detector geometry, the probability of getting a single hit in the wires per neutron is 70%. A single neutron produces hits in two wires about 30% of the time, and hits in four or more wires drops to 1% of the time. For the strips, roughly 50% of the time two strips have a hit[17], and 25% of the hits are from a single strip or three strips. The likelihood of having 4 or more strips involved is less than 1% [10]. The number of hits within a channel sub-cluster is called the "multiplicity". For the analysis done in this thesis, multiplicity limits of 2 for the wires and 3 for the strips were assigned, since the probability of having more than 2 hits simultaneously in the wires and more than 3 hits in the strips is very low. The sub-clusters that did not fulfill the multiplicity requirements were simply rejected. Accepted sub-clusters form main clusters that contain information about the x and y coordinate of the neutron event when $\Delta t = 3$ μs. To first order, the x and y coordinate of a neutron event is determined by the channel that measured the largest signal. This is sufficient for determining the position of the wire or x-coordinate, since most of the events have a wire multiplicity of one or two. By assuming that the signal decreases proportionally with distance from the avalanche point, the strip coordinate precision can be improved by weighting the accumulated charges in the strip [7]. The weighting method is referred to as Center-Of-Gravity (COG):

$$y = \frac{\sum Q_i y_i}{\sum Q_i}, \tag{3.4.2}$$

where Q_i is the recorded charge measured by the strip y_i in the main cluster. In this thesis, a COG algorithm for the strips with first decimal precision was used[18].

[16] ADCch corresponds to ADC channel unit in which the charge of the signal was measured.

[17] The reason for a strip multiplicity distribution varies so drastically from that in the wires is capacitive signal coupling. Explanation of the effect is beyond the scope of this thesis.

[18] The COG can in principle be applied to the wires as well.

Chapter 4

Results and Summary

4.1 Results

4.1.1 2D Images

The reconstructed 2D image from the "ess" mask (Fig. 3.3.2a) measurement is shown in Fig. 4.1.1. Neutrons clearly are attenuated by the mask but pass through the engravings so that "ess" is easily recognizable. The reconstructed 2D images in this thesis have in

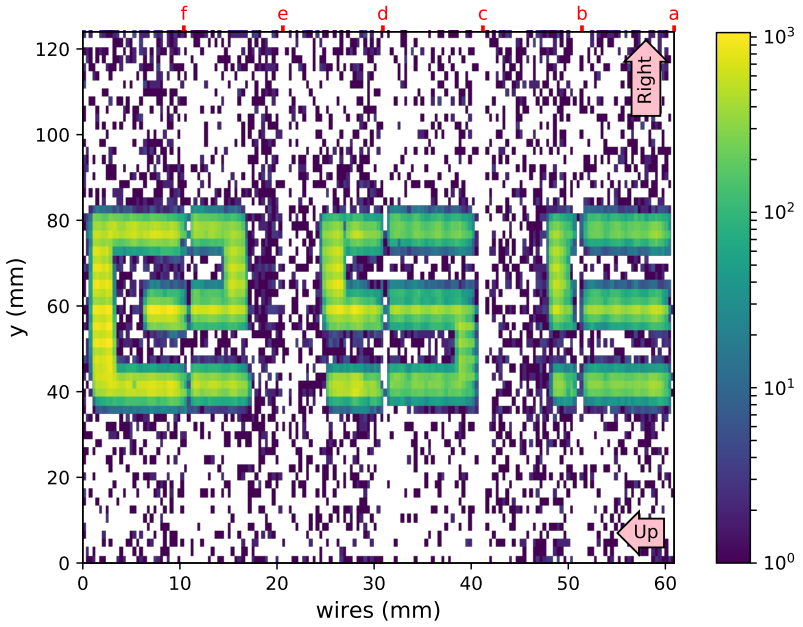

Figure 4.1.1. The "ess" mask measurement reconstruction. The z scale of the reconstruction is logarithmic, and the colors represent the number of counts in a given pixel. The white pixels represent the areas where no hits were detected and dark blue pixels represent background. The arrows in pink represent the orientation of the mask in laboratory.

total $175 \times 64 = 11200$ pixels, where each pixel represents an area of 0.35 (horizontal) $\times$ 2 (vertical) mm^2. The full dimension of the scatter plot 61×124 mm^2 corresponds to the active area of the detector. The "s"-engraving at x = 55 mm is incomplete due to the fact that the sensitive area of the detector is smaller than the physical dimensions of the mask. Figure 4.1.1 has visible vertical "gaps" in the "ess" lettering and in the background distribution, marked by the red letters on top of the plot. These areas are single pixel regions of inefficiency that represent the first wire of each cassette, counted from the front of the blade. The inefficiency is a result of the local electric field geometry in the front part of the cassette, see Sect. 4.1.3.

The "ess" mask measurement has a very encouraging S/N ratio as shown in Fig. 4.1.2, where a 3D representation of the scatter plot is presented. The dark blue pixels represent background. The background is fully two orders of magnitude lower than the detected signal. The background is most probably neutrons scattered in the laboratory environment or internally in the detector.

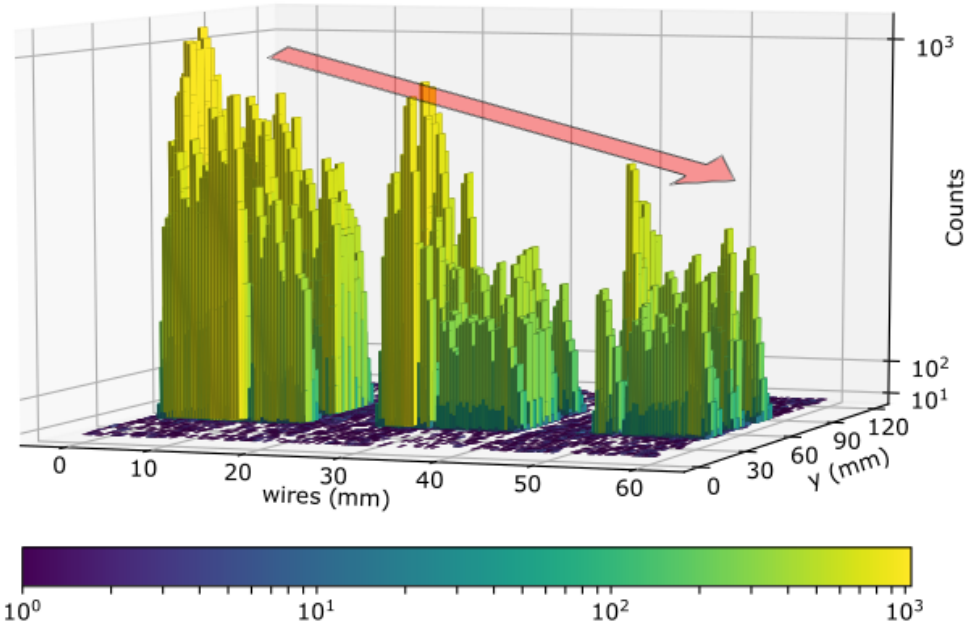

Figure 4.1.2. The "ess" mask measurement 3D representation. The arrow highlights the decreasing gradient from left to right in counts.

There is also a distinctive gradient in the number of counts from the "e" to the second "s" in "ess" as seen in Fig. 4.1.2. There are three factors which contribute to this effect. First, the scanning of the mask started and stopped at the "e" position. The bins are not time normalized as the start and stop of the scan and DAQ both had to be carried out manually. Thus, on average, more counts resulted near the start and stop position of the beam. Second, as seen in Fig. 3.3.1, the reflected neutron beam had an asymmetric spread in the x-direction (lab vertical), with a longer "tail" in the upwards direction. Therefore, the engraving "e" was irradiated continuously throughout the scan. Finally, the measurement was not normalized to neutron energy. Neutron reflection is a function

of λ_n and due to the wide ΔE_n of the neutron beam, the reflection from the supermirror was not uniform throughout the scan. This resulted in a tail in the neutron-energy distribution.

4.1.2 Resolving power

With the mask in Fig. 3.3.2b, a limit on the MB-16 resolution can be measured. The mask had a series of equally sized ø=0.5 mm holes laid out in a symmetric grid formation. The row spacing parallel to the strips was 5 mm while the columns were 2 mm apart. Based on the geometrically projected wire pitch 0.35 mm, MB-16 should be able to resolve the column spacing. Since the projected geometry of the MB-16 blades does not improve the 4 mm strip pitch, the 5 mm gaps between the rows should indicate if the COG method applied during the data analysis results in a strip resolution sufficient to resolve the gap spacing.

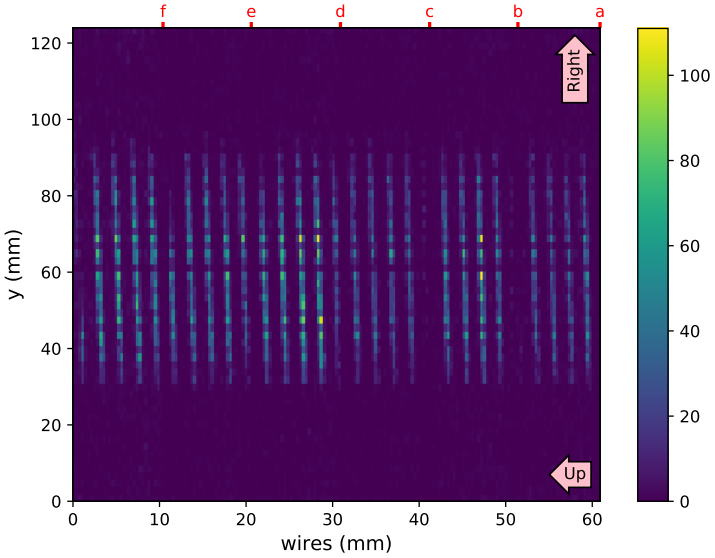

(a) Dotted mask reconstruction. The low statistics are due to the size of the holes in the mask.

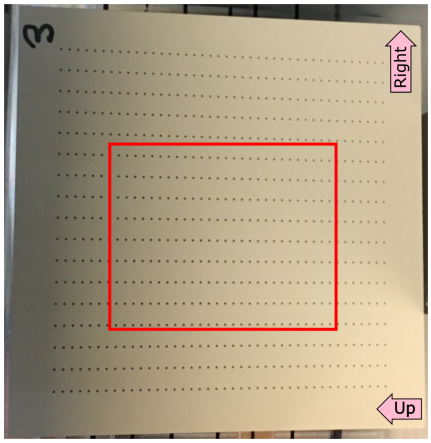

(b) Dotted mask close-up. The region in red illustrates the area scanned with the neutron beam.

Figure 4.1.3. Dotted mask and its 2D reconstruction. The reconstruction is plotted in linear scale to highlight the pattern recognition. The letter labels in red at the top of a) represent the locations of the beginning of a new blade, and thus the first wire from right to left. The pink arrows represent wire, strip and mask orientation during the measurement.

The picture of the mask and the reconstructed 2D image are shown in Fig. 4.1.3. The column spacing of 2 mm is clearly resolved in the reconstruction. To first order, MB-16 is able to resolve structures 2 mm apart in the direction of the wires. Note however that the measurement was not ideal for measuring the resolution of the detector. The beam was divergent and not normalized to time or energy, so definite limit on the resolution of

MB-16 cannot be determined with these results. That said, 2 mm in a single direction is attainable.

The consecutive rows of dots in Fig. 4.1.3a are not resolved, indicated by the coupled dots forming distinctive vertical lines in the reconstruction. The dots in the y-direction (lab horizontal) fuse together and thus demonstrate that the position resolution provided by the strips is larger than 2.5 mm with the applied COG correction. Note that the vertical lines obtained in Fig. 4.1.3a are not exactly orthogonal to the x-axis because the detector was mounted with a slight tilt relative to the mask.

From this analysis, it can be concluded that MB-16 is able to resolve structures separated by 2 mm in the wire direction, but not able to resolve structures that are separated by 5 mm in the strip direction. The 2 mm resolution in the x-direction (lab vertical) is simply a firstpass benchmark. For more precise results, the measurement conditions and methods must be optimized. In addition to time and energy normalization, a well-collimated uniform neutron beam together with a precisely defined mask placement will be necessary. With these in place, it will be possible to determine the limit on the position resolution of the MB-16 detector.

4.1.3 Uniformity

As seen in all of the 2D reconstructions, the images suffer from distinctive inefficiency regions, represented by visible vertical lines of reduced sensitivity. This appears in the signal-distribution region as well as in the background-distribution region of the reconstructions, see Fig. 4.1.4. Due to the geometry and configuration of the blades, MB-16 has no dead areas. Most notably, the "knife"-shaped design in the front end allows for

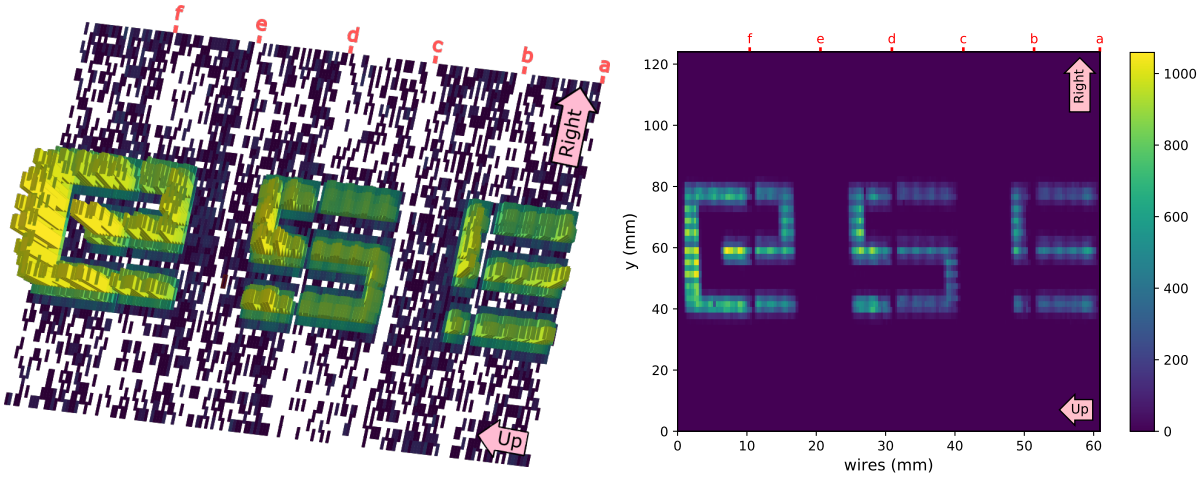

(a) Inefficiency lines in the background distribution.

(b) Inefficiency lines in the engravings.

Figure 4.1.4. Inefficiency lines in the 2D reconstructions. Image a) is plotted on a logarithmic scale and image b) on a linear scale. The pink arrows represent wire, strip and mask orientation during the measurement.

a continuous projected wire spacing for the active area of the detector. A drawback of this is the reduced electric-field strength at the tip of each cassette, which arises from the larger strip-to-wire distance in this region. In addition, the first wire of each cassette closes the electric field. This generates an inhomogeneous field profile and smaller field gradient between the ^{10}B layer and the wire. Thus, the charge multiplication is locally smaller than the normal level of charge multiplication across the full cassette. The reduced sensitivity of the first wires can be compensated for by assigning a lower signal threshold relative to the other wires. However, the limit cannot be set arbitrarily low because of electric noise. In this work, a single software threshold was applied to all of the wires. This suppressed the response of the first wires even further. The lower sensitivity region for MB-16 is 5 mm [10], which is roughly the spacing between wires[19].

As shown in Fig. 4.1.4, the width of the inefficiency lines is not the same over the entire detector. This effect arises because only one blade was aligned to the optimal 5° angle, leaving the other blades decreasingly offset. The shadow areas were thus not equal in size (recall Fig. 2.1.3), and might not correspond to an integer number of the wire pitch. As seen in Fig. 4.1.3a, the detector was also slightly tilted, which increased the width of the objects in the x-direction and thus amplified the inefficiency regions.

4.2 Summary

4.2.1 Overview

The MB will ultimately be used to instrument the ESTIA BL at ESS and be employed for material-surface studies. The MB-16 prototype has been specially designed for thermal-neutron detection with high spatial resolution in a single dimension. The aim of this thesis was to extract for the first time 2D images from data obtained at a neutron reflectometer with the MB-16 prototype of the MB detector. Investigations were performed both at the STF in Lund and at the reflectometry instrument CRISP at the spallation source ISIS in RAL, England. Investigations at the STF included a detailed pre-study of the theory behind the MB design and an introduction to the operation of the MB-16 prototype. Testing of the response of MB-16 to variations in $ArCO_2$ gas blends followed. It was determined that a reduction in the Ar gas concentration required an increase in applied HV to maintain the same gain in the detector. Investigations at ISIS involved irradiating MB-16, a vertical-reflectometry detector, at a horizontal-reflectometry BL. The active area of MB-16 was covered with neutron-absorbing B_4C masks engraved with distinctive physical patterns. Manual, unsynchronized beam scans using a pulsed, divergent neutron beam smaller than the active area of the detector were employed. Neutron drift distances were not optimal. MB-16 showed excellent response, clearly imaging sub-centimeter engravings with a S/N ratio ~ 50. Via COG weighting of the neutron-induced charge in the detector, MB-16 imaged a matrix of regularly spaced holes in the direction perpendicular to the wires. In the direction perpendicular to the strips, the same holes could not be resolved.

[19]The inefficiency in the front end of the blades can be compensated if a higher voltage is separately applied to these electrodes.

MB-16 showed regions of inefficiency which appeared as bands in the reconstructed 2D images. These bands correspond to the first two wires of each cassette. The gain of these first channels is lower than nominal the gain of the cassette due to different electric field intensity and blade front-end geometry profile. The geometry of the blades is necessary for a detector active area without dead zones. In addition to improved controls over the individual wires and strips, further studies of MB-16 will require optimization of the beam parameters at a reflectometry BL better resembling ESTIA.

4.3 Conclusions

We draw the following conclusions about MB-16 response, resolution, and uniformity from the neutron-absorbing mask measurement results:

- **Response** The MB detector is capable of measuring 2D thermal neutron images from sub-centimeter structures. The S/N ratio was obtained to be $\sim$50.
- **Resolution** Using the COG algorithm together with a divergent unoptimized neutron beam, MB-16 is able to resolve $\phi = 0.5$ mm holes with 2 mm separation in the direction perpendicular to the wires. In the direction perpendicular to the strips, the $\phi = 0.5$ mm holes with 5 mm separation cannot be resolved.
- **Uniformity** MB-16 suffers from inefficiency bands where the signal response is locally low. These bands correspond to the first two wires of each cassette. The gain of these first channels is lower than nominal gain of the cassette due to different electric field intensity and the front-end geometry profile of the blade. The geometry of the blades is necessary for a detector active area free from dead zones.

4.3.1 Suggestions for Improvement

There were several limitations to the measurements carried out in this work that need to be addressed in order to obtain more precise results. Some of them arise due to the beamline conditions and some from the detector itself.

- **Drift Distance** The detector-to-sample distance should fulfill the engineered blade alignment requirements. As the detector was not at the design distance, only one blade could be precisely aligned with an optimal angle, leaving the other blades decreasingly offset. A shadowing issue emerged which was unique for each cassette.
- **Detector Alignment** The tilting of the detector as well as the blade-alignment problems could be avoided if the detector designed for vertical reflectometry was used only at a BL designed for vertical reflectometry.
- **Supermirror Controls** If neutron beam scanning is to be used, the BL apparatus software should be compatible with the detector DAQ so that the data from the scans could be normalized.

- **Resolving Power** The report estimates the resolution of the detector through resolving power. This can likely be improved if more sophisticated charge-weighting algorithms are developed.

Appendices

Appendix A

DAQ/User Interface

The DAQ User Interface (UI) script was developed using Python 3.6.1 software [24]. The script reads the relevant DAQ parameter values from an Excel file, which acts as an ersatz graphical user interface (GUI). All the signal-acquisition parameters used by the digitizers are stored in a configuration file, recall Sect. 2.1.2. The file is modified via the UI and all the necessary values are written into the digitizer registers at the beginning of each acquisition. Among other settings, for example, all the individual $64 \times 6 = 384$ channel thresholds are modified, resulting in a lengthy file. The Excel platform was chosen to ensure UI compatibility between different computer operating systems. Examples of the UI are shown in Fig. A1 and Fig. A2.

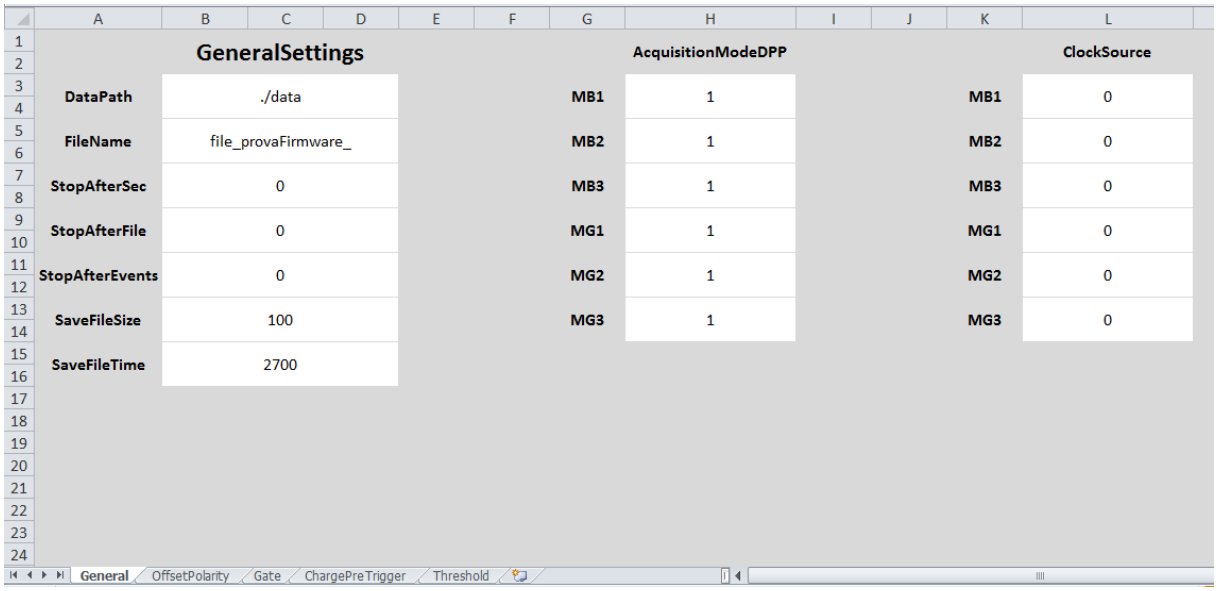

Figure A1. User interface sample image. On bottom left-hand corner of the window the DAQ parameter inputs are accessible.

There are built-in cross-checking functions in the script that flag an error if unphysical or out-of-range values are inserted into the UI. After each modification, a copy of the configuration file with a time stamp is also created for backup purposes.

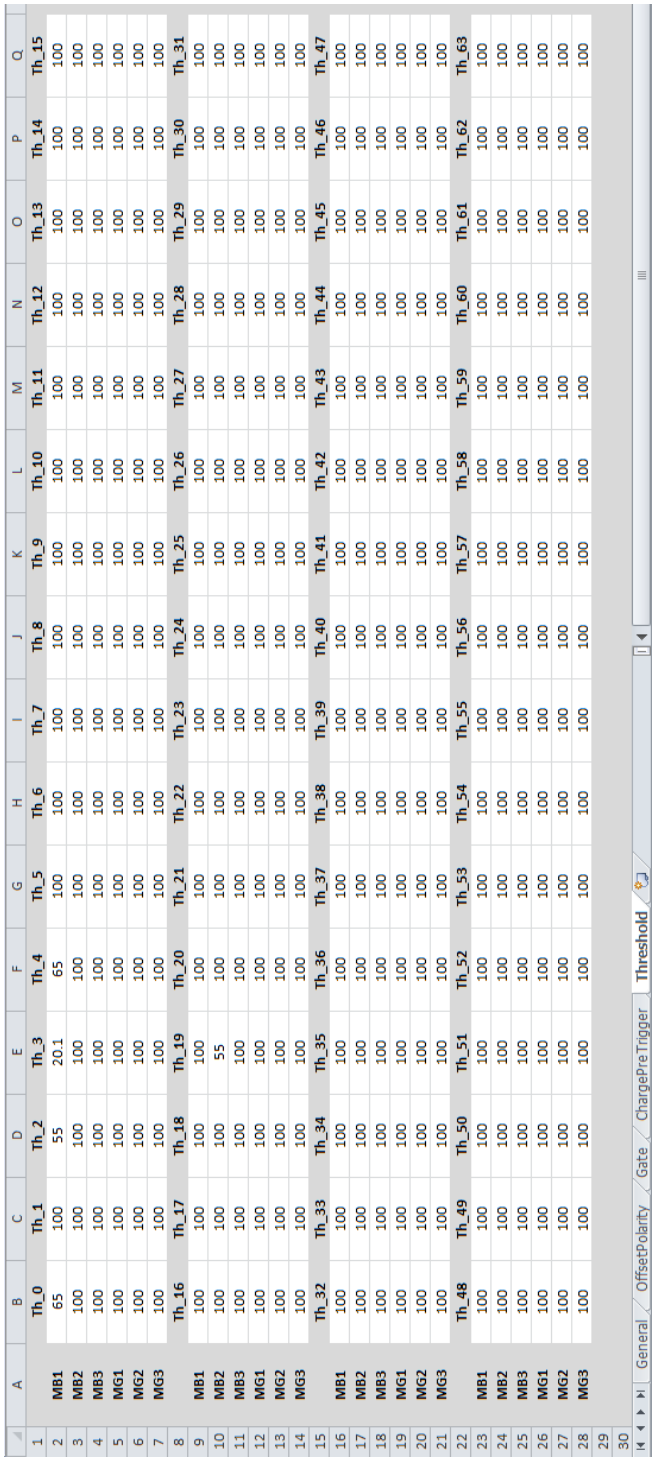

	A	B	C	D	E	F	G	H	I	J	K	L	M	N	O	P	Q
1		Th_0	Th_1	Th_2	Th_3	Th_4	Th_5	Th_6	Th_7	Th_8	Th_9	Th_10	Th_11	Th_12	Th_13	Th_14	Th_15
2	MB1	65	100	55	20.1	65	100	100	100	100	100	100	100	100	100	100	100
3	MB2	100	100	100	100	100	100	100	100	100	100	100	100	100	100	100	100
4	MB3	100	100	100	100	100	100	100	100	100	100	100	100	100	100	100	100
5	MG1	100	100	100	100	100	100	100	100	100	100	100	100	100	100	100	100
6	MG2	100	100	100	100	100	100	100	100	100	100	100	100	100	100	100	100
7	MG3	100	100	100	100	100	100	100	100	100	100	100	100	100	100	100	100
8		Th_16	Th_17	Th_18	Th_19	Th_20	Th_21	Th_22	Th_23	Th_24	Th_25	Th_26	Th_27	Th_28	Th_29	Th_30	Th_31
9	MB1	100	100	100	100	100	100	100	100	100	100	100	100	100	100	100	100
10	MB2	100	100	100	55	100	100	100	100	100	100	100	100	100	100	100	100
11	MB3	100	100	100	100	100	100	100	100	100	100	100	100	100	100	100	100
12	MG1	100	100	100	100	100	100	100	100	100	100	100	100	100	100	100	100
13	MG2	100	100	100	100	100	100	100	100	100	100	100	100	100	100	100	100
14	MG3	100	100	100	100	100	100	100	100	100	100	100	100	100	100	100	100
15		Th_32	Th_33	Th_34	Th_35	Th_36	Th_37	Th_38	Th_39	Th_40	Th_41	Th_42	Th_43	Th_44	Th_45	Th_46	Th_47
16	MB1	100	100	100	100	100	100	100	100	100	100	100	100	100	100	100	100
17	MB2	100	100	100	100	100	100	100	100	100	100	100	100	100	100	100	100
18	MB3	100	100	100	100	100	100	100	100	100	100	100	100	100	100	100	100
19	MG1	100	100	100	100	100	100	100	100	100	100	100	100	100	100	100	100
20	MG2	100	100	100	100	100	100	100	100	100	100	100	100	100	100	100	100
21	MG3	100	100	100	100	100	100	100	100	100	100	100	100	100	100	100	100
22		Th_48	Th_49	Th_50	Th_51	Th_52	Th_53	Th_54	Th_55	Th_56	Th_57	Th_58	Th_59	Th_60	Th_61	Th_62	Th_63
23	MB1	100	100	100	100	100	100	100	100	100	100	100	100	100	100	100	100
24	MB2	100	100	100	100	100	100	100	100	100	100	100	100	100	100	100	100
25	MB3	100	100	100	100	100	100	100	100	100	100	100	100	100	100	100	100
26	MG1	100	100	100	100	100	100	100	100	100	100	100	100	100	100	100	100
27	MG2	100	100	100	100	100	100	100	100	100	100	100	100	100	100	100	100
28	MG3	100	100	100	100	100	100	100	100	100	100	100	100	100	100	100	100
29																	
30																	

Figure A2. Channel threshold settings. All 576 MB-16 channels are accessible in a single page.

Appendix B

CAD Drawings of the Masks

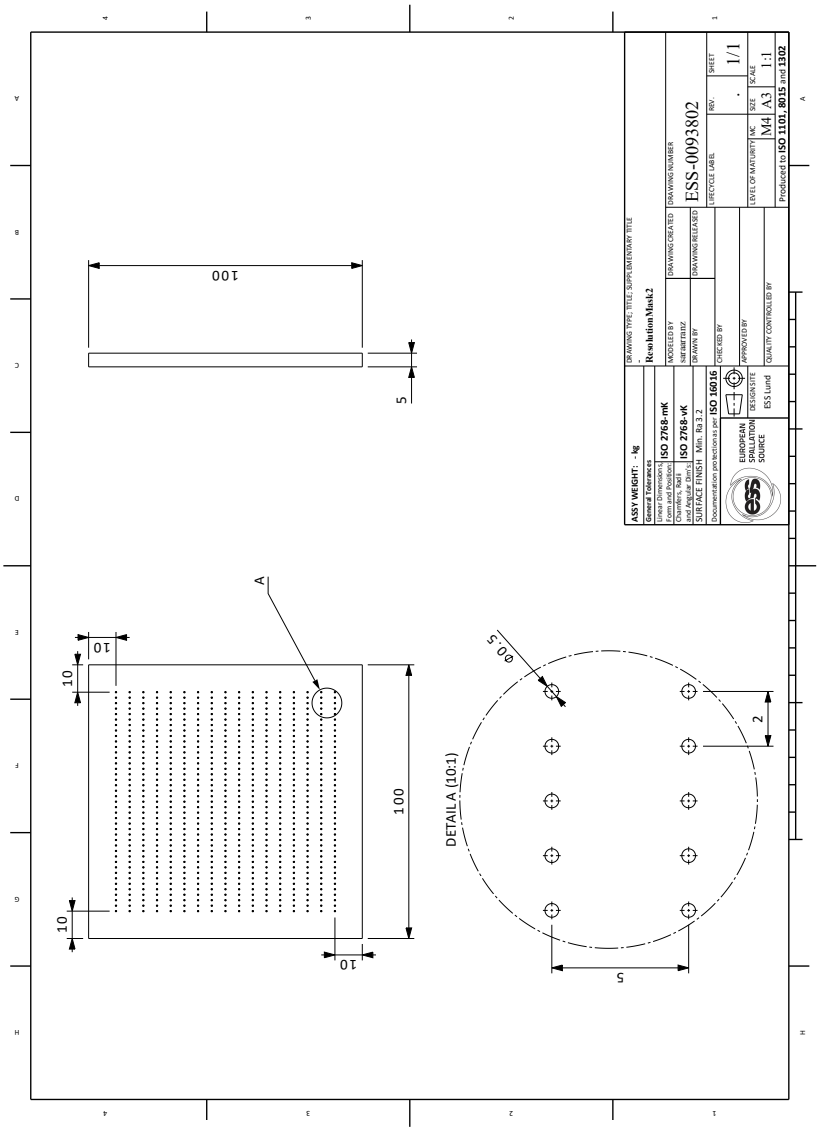

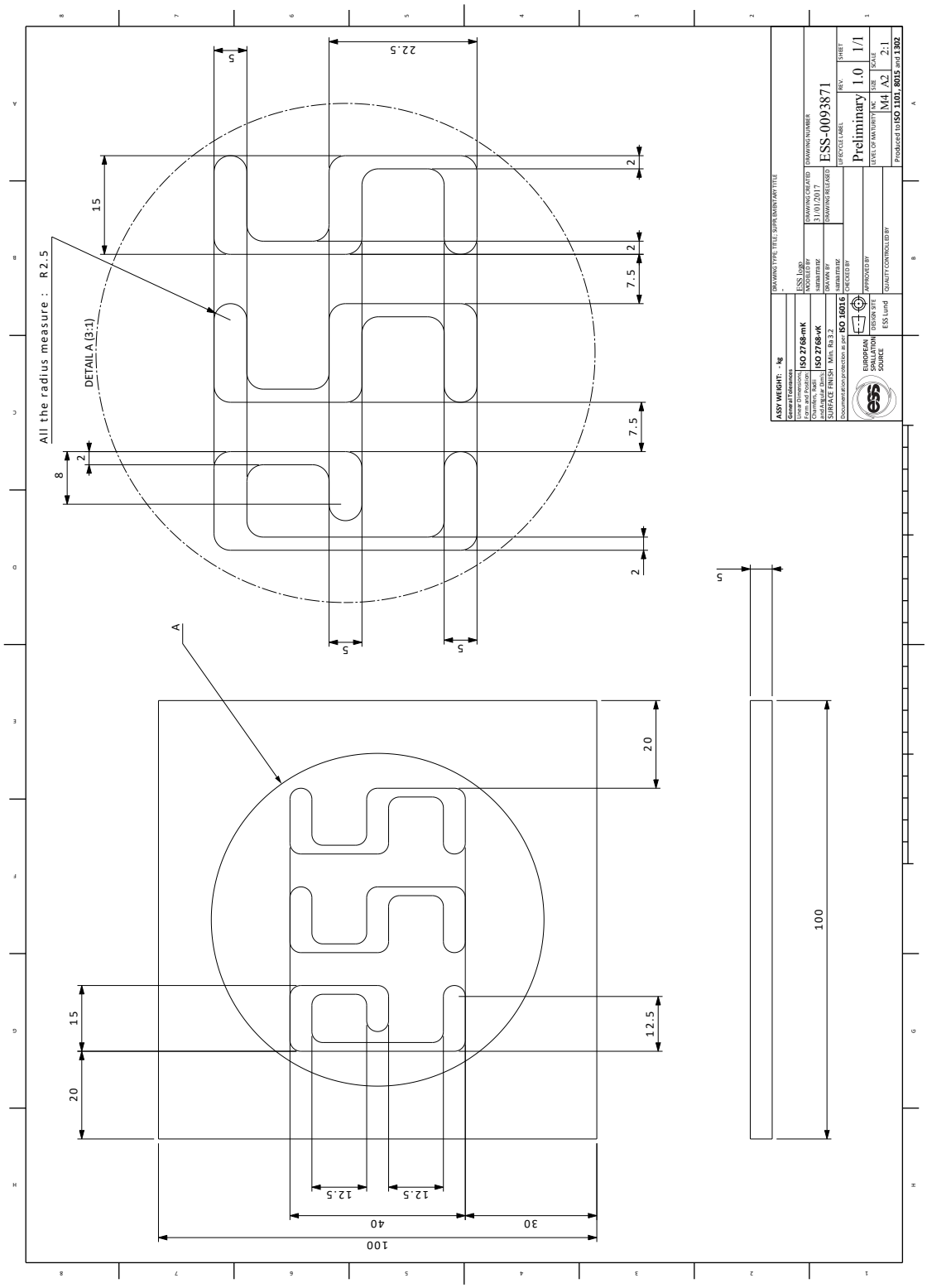
All the radius measure : R2.5
DETAIL A (3:1)
22.5
5
15
2
7.5
8
100
40
30
12.5
20
ESS-0093871
Preliminary
1.0
1/1
M4
A2
2:1
ISO 1101, 8015 and 1302

Appendix C

Contribution of the author

Week	Activity
35	Testing MB-16
36	Background reading
37	Programming UI
38	Programming UI
39	Attended conferences / Programming UI
40	Taking measurements at RAL, England
41	Presentation about the week at RAL
42	Background reading
43	Writing the thesis
44	Programming
45	Programming
46	Data analysis
47	Data analysis
48	Data analysis
49	Data analysis
48	Writing the thesis
49	Writing the thesis
50	Writing the thesis

Bibliography

[1] Kenneth S Krane and David Halliday. *Introductory nuclear physics*, volume 465. Wiley New York, 1988.

[2] James Chadwick. Possible existence of a neutron. *Nature*, 129(3252):312, 1932.

[3] Mark Thomson. *Modern particle physics*. Cambridge University Press, 2013.

[4] Samuel Glasstone and Philip J Dolan. Effects of nuclear weapons. Technical report, Department of Defense, Washington, DC (USA); Department of Energy, Washington, DC (USA), 1977.

[5] Stefaan Tavernier. *Experimental techniques in nuclear and particle physics*. Springer Science & Business Media, 2010.

[6] D A Shea and D Morgan. The helium-3 shortage: Supply, demand, and options for congress. Congressional Research Service, Library of Congress, 2010.

[7] William R Leo. *Techniques for nuclear and particle physics experiments: a how-to approach*. Springer-Verlag, 1994.

[8] G Charpak, R Bouclier, T Bressani, J Favier, and Č Zupančič. The use of multiwire proportional counters to select and localize charged particles. *Nuclear Instruments and Methods*, 62(3):262–268, 1968.

[9] A Khaplanov, F Piscitelli, J-C Buffet, J-F Clergeau, J Correa, P van Esch, et al. Investigation of gamma-ray sensitivity of neutron detectors based on thin converter films. *Journal of Instrumentation*, 8(10):P10025, 2013.

[10] F Piscitelli, F Messi, M Anastasopoulos, T Bryś, F Chicken, et al. The multi-blade boron-10-based neutron detector for high intensity neutron reflectometry at ess. *Journal of Instrumentation*, 12(03):P03013, 2017.

[11] M Åberg, N Ahlfors, R Ainsworth, C Alba-Simionesco, S Alimov, et al. *ESS technical design report*. European Spallation Source, 2013.

[12] Roger Pynn. Neutron scattering by rough surfaces at grazing incidence. *Physical Review B*, 45(2):602, 1992.

[13] F Piscitelli, JC Buffet, JF Clergeau, S Cuccaro, B Guérard, et al. Study of a high spatial resolution 10b-based thermal neutron detector for application in neutron reflectometry: the multi-blade prototype. *Journal of Instrumentation*, 9(03):P03007, 2014.

[14] JC Buffet, JF Clergeau, RG Cooper, J Darpentigny, A De Laulany, et al. Advances in detectors for single crystal neutron diffraction. *Nuclear Instruments and Methods in Physics Research Section A: Accelerators, Spectrometers, Detectors and Associated Equipment*, 554(1):392–405, 2005.

[15] JC Buffet, J Correa, P Van Esch, B Guerard, A Khaplanov, and F Piscitelli. Study of a 10 b-based multi-blade detector for neutron scattering science. In *Nuclear Science Symposium and Medical Imaging Conference (NSS/MIC), 2012 IEEE*, pages 171–175. IEEE, 2012.

[16] CAEN SpA. Technical Information Manual: Mod. v1740 64 channel 12bit - 65ms/s digitizer. Technical report, May 2016.

[17] Tektronix. Triggering Fundamentals With Pinpoint® Triggering and Event Search Mark for DPO7000. Technical report, July 2011.

[18] CAEN SpA. Modular Pulse Processing Electronics / Waveform Digitizers. `http://www.caen.it/servlet/checkCaenDocumentFile?Id=9532`, 2014.

[19] ISlS Neutron and Muon Source. Characteristics of a pulsed source. `https://www.isis.stfc.ac.uk/Pages/Characteristics-of-a-pulsed-source.aspx`. Accessed: 2017-11-29.

[20] F Messi, H Perrey, K Fissum, M Akkawi, R Al Jebali, et al. The neutron tagging facility at Lund University, 2017.

[21] T Krist, A Teichert, R Kovács-Mezei, and L Rosta. *Modern developments in x-ray and neutron optics*, volume 137. Springer, 2008.

[22] CJ Kinane, RM Dalgliesh, S Langridge, and DG Bucknall. CRISP Instrument Manual. `https://www.isis.stfc.ac.uk/Pages/crisp-instrument-manual-nov-2010.pdf`, November 2010.

[23] F Messi, F Piscitelli, and G Mauri. Personal communication, November 2017.

[24] Python Core Team. Python: A dynamic, open source programming language. `http://www.python.org/`, 2015.

The project reported on in this thesis
was performed by

The Multi-Blade Group

in collaboration with

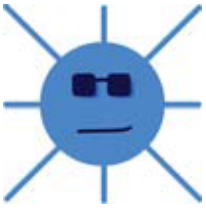

The Source-based Neutron Irradiation Group of the
Division of Nuclear Physics at Lund University

and

The Detector Group of the European Spallation Source ERIC

with support from

The Horizon 2020 BrightnESS Project, Proposal ID 676548